Polar Meteorology

6

Carleen Reijmer, Michiel van den Broeke, and Willem Jan van de Berg

6.1 Introduction

Inhomogeneous heating of the Earth's surface by solar radiation in space and time introduces horizontal and vertical temperature and thus density gradients. These density gradients lead to pressure gradients that cause air flow, which in turn influences temperature and pressure, resulting in a complex system of forcing and feedbacks that determine the state of the atmosphere.

The polar atmosphere differs from the mid-latitude and tropical atmosphere in that it endures the most extreme seasonal insolation variations on Earth, with an absence of solar radiation in winter (Polar Night) to 24 hours of daylight in summer (Polar Day). In terms of surface characteristics (land/sea distribution, elevation, surface roughness, vegetation, etc.), the Arctic and Antarctic regions are very different: the Arctic is an ocean surrounded by continents, the Antarctic a continent surrounded by oceans (Fig. 6.1). In the Arctic region, poleward of 70° N, only 30% of the surface is land, while in the Antarctic region the corresponding amount is 72%. The Antarctic continent is almost completely (∼ 99%) covered by an ice sheet, resulting in it being the highest continent on Earth with an average elevation of ∼ 2100 m above sea level (a.s.l.). While most of the sea ice in the Antarctic region is relatively thin single-year ice, the Arctic Ocean is partly covered by thicker multi-year sea ice that has survived at least one summer.

In this chapter, a brief introduction to atmospheric radiative theory is given, followed by a discussion of the general characteristics of the polar atmosphere in terms of the (surface) energy budget, large-scale flow patterns and related features such as precipitation, the near surface temperature inversion and katabatic flow. The

C. Reijmer (✉) · M. van den Broeke · W. J. van de Berg
Utrecht University, Utrecht, The Netherlands
e-mail: c.h.tijm-reijmer@uu.nl

A. Fowler and F. Ng (eds.), *Glaciers and Ice Sheets in the Climate System*, Springer Textbooks in Earth Sciences, Geography and Environment,
https://doi.org/10.1007/978-3-030-42584-5_6

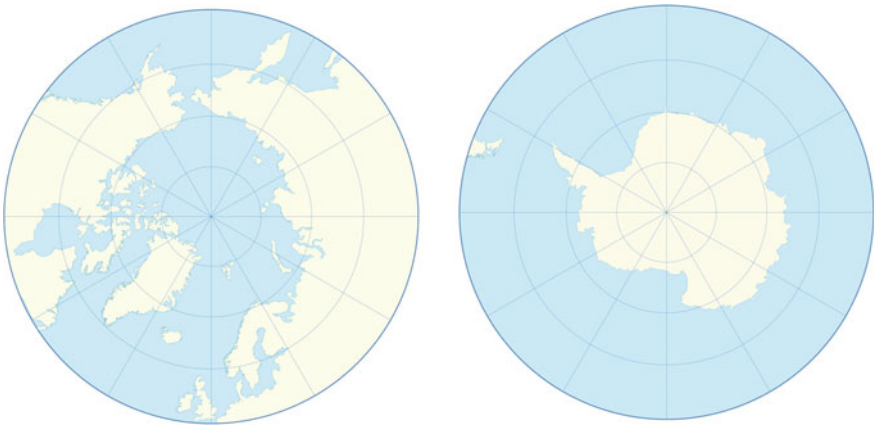

Fig. 6.1 Maps of the Arctic and Antarctic regions

characteristic features of the polar atmosphere will be highlighted and the differences between the Arctic and Antarctic regions discussed.

6.2 Shortwave and Longwave Radiation

Each body with a temperature above absolute zero, including the Sun and Earth, emits and absorbs electromagnetic radiation. The intensity of emitted radiation is, to first order, described by the laws for black body radiation, which refer to a hypothetical body that absorbs all radiation and has maximum emissivity in all directions. The intensity of black body radiation emitted from a surface as a function of wavelength λ is given by the Planck function

$$F_\lambda(T) = \frac{2\pi hc^2}{\lambda^5 \left(e^{hc/k\lambda T} - 1\right)}, \tag{6.1}$$

where $F_\lambda(T)$ (W m^{-3}) is the monochromatic flux density (per unit wavelength) or monochromatic irradiance[1] as a function of emission temperature T. In this expression, h is Planck's constant, k is Boltzmann's constant and c is the speed of light. (Values of these and other constants are given in Table 6.2 at the end of this chapter.)

[1] The Planck function at a point gives the radiative intensity per unit solid angle as a function of direction: the factor of π in (6.1) arises at a surface when this is integrated over a half-sphere of directions away from the surface. Thus the emitted intensity at a point as a function of direction is F_λ/π.

By integrating (6.1) over the wavelength domain, the total flux density or total irradiance $F(T)$ (W m^{-2}) is obtained ([1], p. 123):

$$F(T) = \int_0^\infty F_\lambda(T)\, d\lambda = \int_0^\infty \left[\frac{2\pi hc^2}{\lambda^5 \left(e^{hc/k\lambda T} - 1\right)} \right] d\lambda = \sigma T^4. \tag{6.2}$$

This is the Stefan–Boltzmann law, where σ is the Stefan–Boltzmann constant. It states that the radiation flux emitted by a black body is proportional to the fourth power of the absolute temperature in Kelvin. A body that is in thermodynamic equilibrium with its surroundings emits all radiation that is absorbed, i. e., its emissivity ε equals its absorptivity. For a black body, emissivity and absorptivity equal 1. In general this does not hold for natural surfaces (grey bodies), where $\varepsilon < 1$ (also note that ε depends on wavelength). For most natural surfaces, the broadband (wavelength-integrated) value of ε ranges between 0.9 and 1. The general expression for emitted radiative flux for grey bodies then becomes

$$F(T) = \varepsilon \sigma T^4. \tag{6.3}$$

In the atmosphere we observe a mix of solar and terrestrial radiation. The Sun emits radiation representative of a temperature of about 5,780 K, compared to a radiative temperature of $\sim$255 K for the Earth-atmosphere system. Owing to the proportionality to the fourth power of absolute temperature of the emitting source, both radiation types are well separated in the wavelength domain (Fig. 6.2) and only have a small overlap at about 5 microns. It is therefore common to distinguish between solar or shortwave radiation (Shw) and terrestrial or longwave radiation (Lw). In discussing radiative fluxes in the climate system it is furthermore common to integrate the radiative flux density at a point, F_λ/π, over either the upward- or downward-facing directional hemisphere in order to distinguish between downward (incoming) and upward (outgoing/reflected) radiation ($Shw_{\text{in}}, Shw_{\text{out}}, Lw_{\text{in}}, Lw_{\text{out}}$).

6.3 Radiation Climate at the Top of the Atmosphere

The average instantaneous energy flux received from the Sun at the top of the atmosphere (ToA) is $S_0 \sim$1366 W m^{-2}, which is proportional to the area under the curve in Fig. 6.2. S_0 is the solar constant, which in reality shows small ($< 1\%$) fluctuations due to variation of the the distance between Earth and Sun, and to vagaries of solar physics, notably the sunspot cycle. The total energy intercepted by the Earth, when distributed evenly over the globe and averaged over the year, is $S_0/4 \sim 341$ W m^{-2}. $S_0/4$, the insolation at ToA, is the average rate at which the Earth and its atmosphere receive solar radiation, and emit radiation back to space, assuming the Earth-atmosphere system to be in radiative equilibrium with the Sun.

The annual global average energy balance of the Earth-atmosphere system is presented in Fig. 6.3. Three levels can be distinguished: the top of the atmosphere (ToA), the atmosphere itself (represented as a single layer) and the surface of the

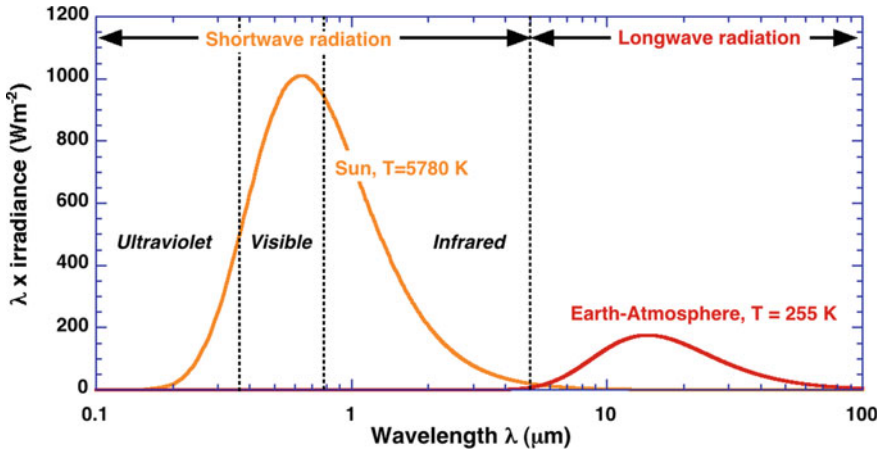

Fig. 6.2 Black body spectra representative of the (incoming) radiation temperature of the Sun ($\sim$5780 K) at Top of the Atmosphere (ToA) and the (outgoing) radiation temperature of the Earth's atmosphere ($\sim$255 K). Wavelength (λ) is plotted on a (base 10) logarithmic scale to enable presentation of both curves in one plot. The irradiance F_λ is multiplied by λ in order to make the area below the curves proportional to the wavelength integrated irradiance $F(T)$. The total received solar radiation at ToA is 1366 W m^{-2}. The area under the Earth curve is smaller than that under the Sun curve by a factor $\frac{1}{4}(1-\alpha) \approx 0.17$, where α is the albedo (the fraction of reflected incoming radiation), and the factor of $\frac{1}{4}$ is due to the receipt of incoming radiation over an area πR_E^2, but emission over an area $4\pi R_E^2$, where R_E is the Earth's mean radius. See also Exercise 6.2

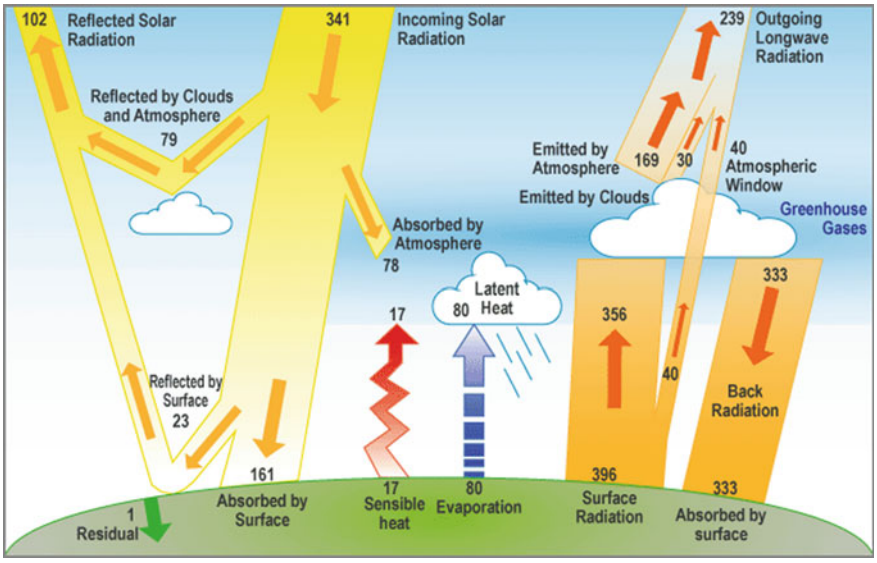

Fig. 6.3 The energy balance of the Earth-atmosphere system, globally and annually averaged. Diagram adapted from (and its numbers based on) Trenberth et al. [2]

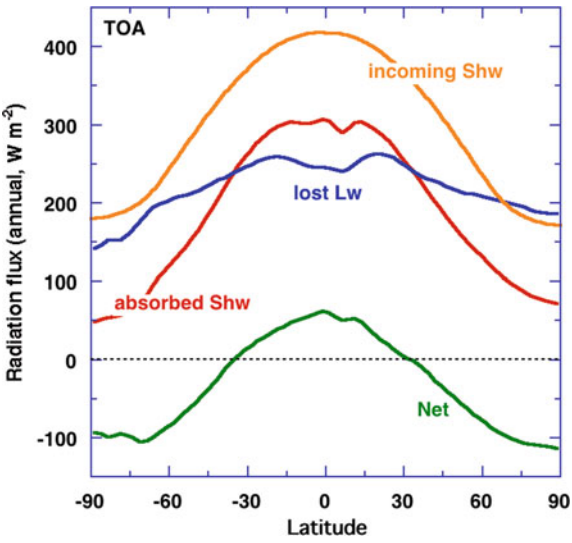

Fig. 6.4 The annually averaged radiation balance at the top of the atmosphere from satellite observations [3]

Earth. For instance, the figure shows that there is radiation balance at the top of the atmosphere but not at the other two levels (why not?).

Figure 6.3 shows that the Earth-atmosphere system is not absorbing all energy provided by the Sun; part of it is reflected back to space, mainly by clouds, with smaller contributions from the surface and aerosols in the troposphere (the lowest 10–15 km of the atmosphere). Note that, like emissivity, reflectivity is wavelength dependent. When integrated over the shortwave spectrum, the broadband reflectivity or broadband albedo for shortwave radiation is defined as:

$$\alpha = \frac{Shw_{\text{out}}}{Shw_{\text{in}}} \,. \tag{6.4}$$

When evaluated at ToA α is called the planetary albedo α_p; when evaluated at the surface, α is called the surface albedo α_s. Note that surface albedo is an important component of planetary albedo. Averaged over the globe, $\alpha_p \sim 0.31$ and $\alpha_s \sim 0.17$, as estimated from satellite observations (see also Fig. 6.3).

The solar constant S_0 represents the upper bound of shortwave radiation to be received at the Earth's surface, if solar incidence is normal and no atmosphere would be present. In the present Sun-Earth configuration, annual average ToA incoming solar radiation is a function of latitude, while instantaneous ToA incoming solar radiation is also a function of time of day (or longitude) and time of year. The zonal distribution of annual average radiation balance at ToA is illustrated in Fig. 6.4. The figure shows that the atmosphere experiences approximate radiative balance only at about 30° N and 30° S. In the tropics (30° S to 30° N), absorbed shortwave radiation exceeds the lost longwave radiation, i. e., there is a radiation surplus, while there is a radiation deficit poleward of these latitudes. The geographic poles receive about 40% of the shortwave radiation received at the equator. The flattening of the absorbed shortwave radiation curve is due to high average cloud cover in

the equatorial region (the Inter-Tropical Convergence Zone, ITCZ) resulting in less absorption of shortwave radiation. The geographical differences between the Arctic and Antarctic regions become apparent in the higher values of lost longwave radiation in the Arctic region caused by relatively high temperatures due to lower surface elevation compared to the Antarctic region. The strong gradient in net absorbed radiation in Fig. 6.4 is balanced by horizontal oceanic and atmospheric equator-pole heat transport.

6.4 Large Scale Circulation

In response to the differential heating/cooling of the atmosphere, there is a negative equator-to-pole tropospheric temperature gradient. Since we expect the thickness of an atmospheric layer to be proportional to its temperature[2], this temperature gradient results in a gradient in the height of atmospheric pressure levels. Figure 6.5 shows this gradient for the 500 hPa level. Away from the surface, the resulting pressure gradient balances the Coriolis force, resulting in a geostrophic westerly flow on both hemispheres. The strongest westerlies are found in the winter at mid-latitudes when the meridional temperature gradients are largest. Also in the large scale circulation the contrast between the Arctic and Antarctic regions becomes apparent. These differences mainly result from the different land/sea distribution in both hemispheres.

Since the static and dynamic (mixing) heat capacity of the ocean is much larger than that of land surfaces, radiative cooling is strongest over the continents. The resulting local steepening of the temperature gradient over the Northern Hemisphere (NH) continents introduces asymmetries in the zonal temperature distribution. This is reflected in the larger gradient of the 500 hPa height over the NH continents (Fig. 6.5) which is strongest in winter near the eastern edges of the continents where the horizontal temperature gradients are largest. A consequence of this local steepening is a displacement of the circumpolar flow out of zonal symmetry. These quasi-stationary structures are called stationary planetary waves, and are preferred regions for cyclone development. These asymmetries largely disappear in summer, when land/sea temperature gradients are more modest.

In the Southern Hemisphere (SH) the pattern is less disturbed by the presence of continents. There is a slight asymmetry caused by the off-pole location of the Antarctic continent. The zonal structure does not change much through the year, but the meridional temperature gradient is strongest in winter. Because of the high elevation of the Antarctic Ice Sheet, temperatures throughout the troposphere are influenced by the cold surface. As a result, the meridional temperature gradient in the SH is larger than in the NH. As a rule of thumb, it is fair to say that the summer gradient in the 500 hPa surface in the SH is comparable to the winter gradient in the NH. Note that the apparent zonal symmetry is misleading, as cyclones are

[2] Because of the perfect gas law.

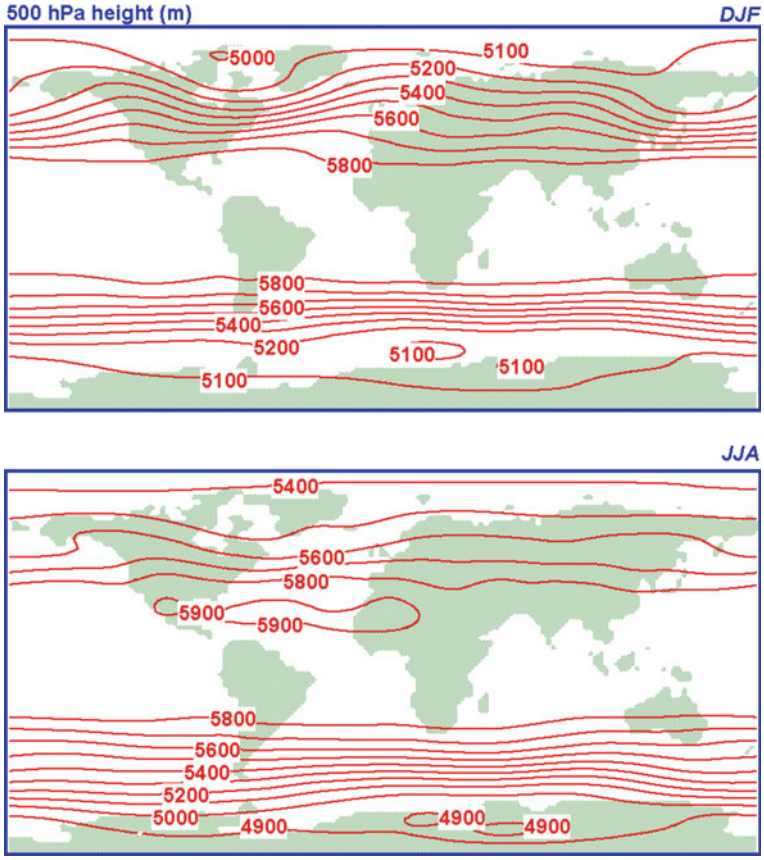

Fig. 6.5 Average geopotential height of the 500 hPa level for December, January, February (DJF) (top panel) and June, July, August (JJA) (bottom panel) (based on ECHAM4 data)

continuously developing, more frequently at the eastern edges of the continents, after which they migrate south-eastwards towards the Antarctic continent.

At the surface level, climate differences between the Arctic and Antarctic regions are also evident. In the NH the distribution of the storm tracks is dominated by the land/sea distribution, resulting in the climatological Icelandic Low over the North Atlantic ocean and Aleutian Low in the North Pacific. Over the North Polar basin, in the absence of strong temperature gradients, atmospheric pressure gradients are relatively weak in both seasons. In winter (Fig. 6.6, left), the Icelandic Low creates a pressure gradient across the Arctic basin, resulting in mean eastward flow from Asia towards Greenland. It forces a transpolar current from Asia to America over the North Pole, which is why the thickest sea ice is found on the north coast of the Canadian Arctic and Greenland.

In the absence of large land masses in the region between Antarctica and south of 40° S, a continuous circumpolar pressure trough (CPT) develops in the SH (Fig. 6.6, right). Low pressure systems cannot penetrate the high Antarctic interior and decay

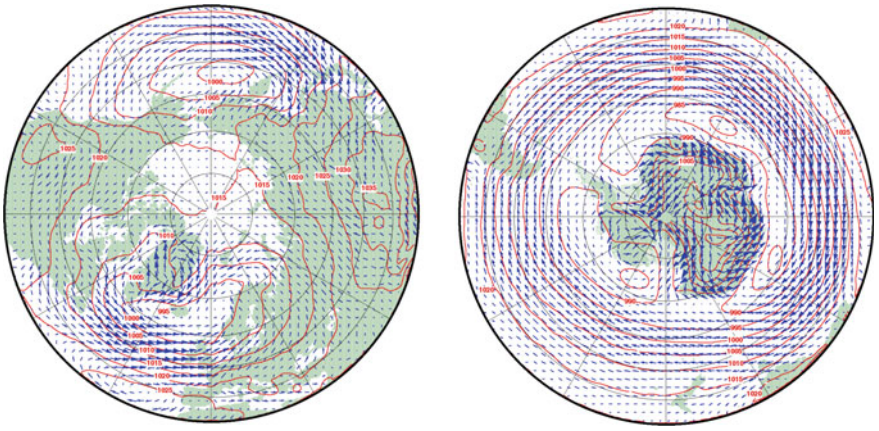

Fig. 6.6 Mean Arctic and Antarctic winter (DJF and JJA, respectively) sea level pressure and 10 m wind vectors (longest vector corresponds to 10 m s^{-1}) (based on ECHAM4 data)

close to the Antarctic coastline, resulting in the climatological CPT. Preferred locations for low pressure areas to end up at the Antarctic coastline are found around 30° E, 110° E and 150° W; these are probably associated with indentations in the Antarctic topography. The westerly circulation is well established near the surface, with an annual mean wind speed of about 10 m s^{-1} at the 10 m level (Fig. 6.6, right). An interesting implication of the CPT is that the surface winds as well as the coastal currents are easterly along the Antarctic coastline.

Over the Greenland and Antarctic Ice Sheets a well-developed anticyclonic circulation is present near the surface, which is stronger in winter than in summer and peaks over the steepest slopes. The associated katabatic winds will be discussed in Sect. 6.6.

6.5 Surface Energy Balance

Averaged over the year and globe there is radiation balance at the ToA, but not so in the atmosphere or at the surface (Fig. 6.3). About 55% of the incoming shortwave radiation at the ToA reaches the surface, where most of it ($\sim$85%) is absorbed. The absorbed shortwave radiation heats the surface and in turn the surface emits longwave radiation to the atmosphere. Most of the emitted longwave radiation is absorbed in the atmosphere, which in turn emits longwave radiation to space and back towards the surface. As a result of this *greenhouse effect*, the net longwave loss at the surface is relatively small and does not balance the absorbed short wave radiation. The surface (and atmospheric) energy balance is closed by the surface turbulent fluxes of sensible and latent heat.

If we consider the energy balance of a surface 'skin' layer, conservation of energy dictates that all fluxes must balance, because the skin layer is infinitesimally thin with zero heat capacity. For a single location and in case of a snow/ice covered surface

the surface energy balance can be written as the sum of melt energy (M), shortwave radiative fluxes (Shw), longwave radiative fluxes (Lw), turbulent fluxes of sensible (H) and latent heat (LE) and the sub-surface heat flux (G_s) (all in W m^{-2}):

$$\begin{aligned} M &= Shw_{\text{in}} + Shw_{\text{out}} + Lw_{\text{in}} + Lw_{\text{out}} + H + LE + G_s \\ &= Shw_{\text{in}}(1 - \alpha_s) + Lw_{\text{in}} + Lw_{\text{out}} + H + LE + G_s \\ &= Shw_{\text{net}} + Lw_{\text{net}} + H + LE + G_s \\ &= R_{\text{net}} + H + LE + G_s. \end{aligned} \tag{6.5}$$

Since M is the energy used for melt, $M = 0$ when the surface temperature $T_s < 273.15$ K. Shw_{in}, Shw_{out} and Shw_{net} are the incoming, reflected and net (absorbed) shortwave radiation, α_s is the surface albedo, Lw_{in}, Lw_{out} and Lw_{net} are the incoming, outgoing and net longwave radiation, R_{net} is the (combined short- and long-wave) net radiation. All fluxes are evaluated at the surface, and fluxes towards the surface are defined positive. Equation (6.5) is equivalent to (2.3) of Chap. 2.

6.5.1 Shortwave Radiation

The global distribution of the net (absorbed) surface shortwave radiation exhibits a zonally rather symmetric distribution (Fig. 6.7a), which is the result of the change in solar incident angle towards the poles. However, the relative decrease of the net shortwave radiation received at the surface near the poles is stronger than that received at ToA, and this is caused by the high surface albedo in the polar regions. While at ToA the polar regions receive about 40% of the shortwave radiation compared to the equator, at the surface this fraction reduces to 20%.

The atmosphere over the polar regions is in general clean and dry, because there are no significant sources of dust or pollution nearby, and the low temperatures induce low moisture content. Over the large ice sheets the atmosphere is also reasonably thin and the cloud cover low. As a result, 70–90% of the insolation at the top of the atmosphere reaches the surface. Because of the low cloudiness and high transmissivity of the polar atmosphere, the surface albedo becomes the main component of the planetary albedo.

6.5.2 Surface Albedo

The surface albedo is an extremely important component of the surface energy balance, because it determines how much solar radiation can be used to heat the surface, from where it affects all other energy balance components (which all depend on surface temperature). The albedo of snow and ice is generally high, ranging from 0.4 for ice to 0.9 for clean dry fresh snow (Table 6.1). The surface albedo is high over dry snow surfaces such as found in the interior of Greenland and Antarctica, about 0.85, and lower in warmer areas where melt occurs, such as the margins of the Greenland Ice Sheet, where it is 0.4–0.5 (Fig. 6.8). The snow and ice albedoes depend on several

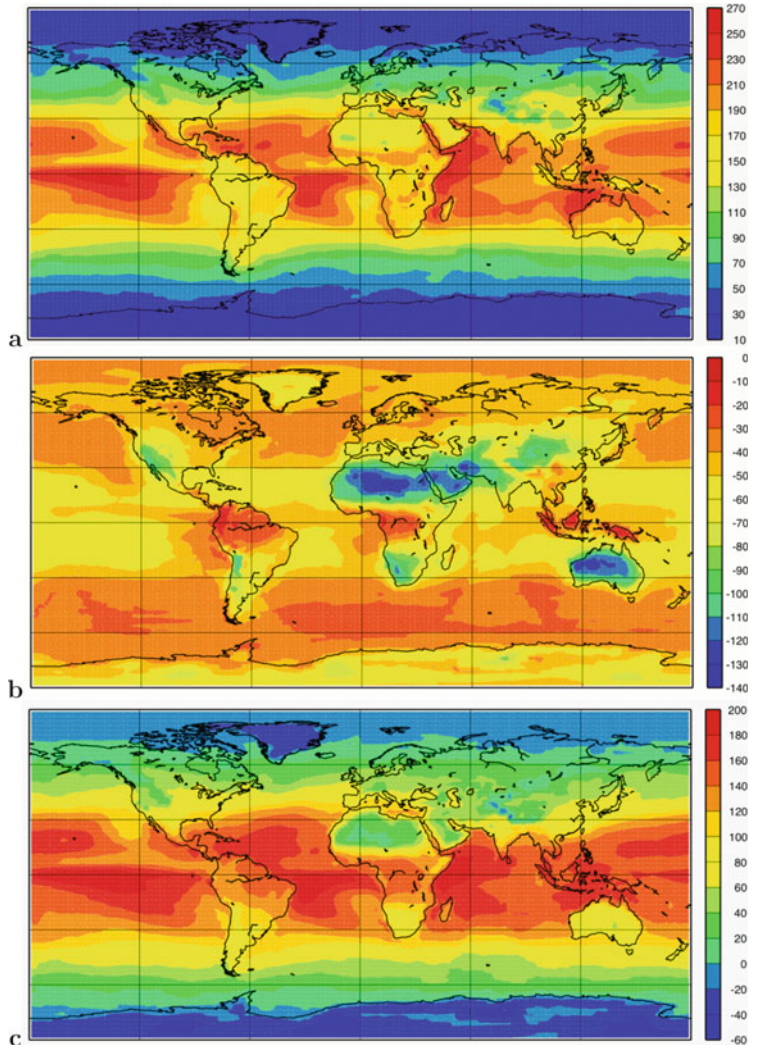

Fig. 6.7 Global annual surface radiation. **a** Net incoming short wave radiation, **b** net incoming (thus negative) long wave radiation, and **c** net incoming all wave radiation based on satellite observations [3]

different factors: solar zenith angle, cloud cover, snow grain size, and impurity/soot content. Especially the latter two result in a positive feedback on melting.

The effective grain size of freshly fallen snow is about 0.05 mm, which will increase in time due to variations in temperature to values of 1–5 mm for old snow. In general, the larger the grain size, the lower the albedo, therefore the albedo decreases in time due to ageing of the snow, resulting in more absorption of shortwave radiation. This constitutes a strong positive feedback on snow melting, because the albedo tends to decrease even faster once melting has occurred. A similar feedback mechanism

Table 6.1 Typical albedo values for different surfaces

Surface	Albedo	
	Min.	Max.
Fresh snow	0.80	0.90
Old snow	0.70	0.80
Firn	0.43	0.69
Clean glacier ice	0.34	0.51
Dirty glacier ice	0.15	0.25
Ocean water	0.03	0.25
Bare rock	0.15	0.30
Grassland	0.16	0.20

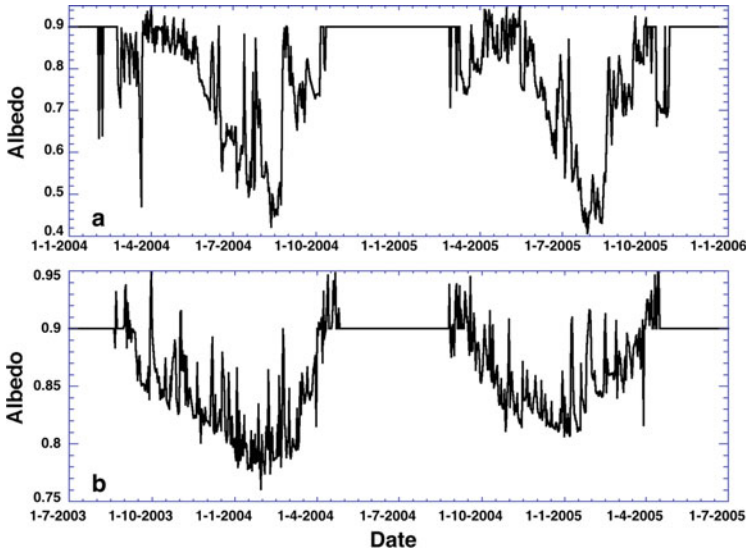

Fig. 6.8 Surface albedo observations on **a** site S6 in the western Greenland ablation area (1100 m a.s.l.) and **b** site AWS 6 in Dronning Maud Land, Antarctica, based on daily averages of shortwave incoming and reflected radiation [4,5]

occurs when melting of snow exposes bare ice, since bare ice has on average a lower albedo than snow. The presence of impurities, soot, and/or debris cover lowers the albedo even further and increases melt, unless the debris cover is thick enough to completely insulate the surface from the effect of solar radiation. Figure 6.8a illustrates these processes for a site on the ablation zone of the Greenland Ice Sheet, where no debris cover is present.

On the cold Antarctic plateau the variations in albedo are mainly the result of ageing of the snow and the effect of changing solar zenith angle. The solar zenith angle determines how far the radiation penetraties the surface; the larger the zenith angle, the less penetration and the higher the albedo. As a result, the albedo exhibits

both diurnal (not shown) and annual cycles, with lowest values at mid-day and mid-summer when solar zenith angle is lowest. The seasonal effect is clearly visible in Fig. 6.8b, which presents albedo observations for a site at about 1100 m a.s.l. in Dronning Maud Land, Antarctica.

6.5.3 Longwave Radiation

According to the Stefan-Boltzmann law for grey surfaces (6.3), the longwave radiation balance is determined by the temperature of the emitting surfaces and its emissivity. Thus, the contribution of the longwave radiation to the surface energy balance is given by

$$Lw_{\text{net}} = Lw_{\text{in}} + Lw_{\text{out}} = \varepsilon_a \sigma T_a^4 - \varepsilon_s \sigma T_s^4, \tag{6.6}$$

where the subscript a denotes atmosphere and s denotes the surface. The emissivity of a snow surface ε_s is typically 0.96–1.0. The downward longwave radiative flux results from emission by the atmosphere, including clouds. Low clouds radiate as black bodies at their (high) cloud base temperature. The clear sky downward longwave flux is determined by the atmospheric temperature profile and the presence of gases (e. g., water vapour and CO_2), which absorb and emit longwave radiation. When expressing the clear sky longwave radiation in terms of the air temperature near the surface, which is readily measured, one can assume that the emissivity of a clear polar atmosphere is about 0.6–0.7.

The global distribution of net longwave radiation at the surface is fairly homogeneous compared to the distribution of absorbed shortwave radiation (Fig. 6.7b). Net longwave radiation is strongly negative in areas where cloudiness is low, which limits the downward longwave radiation flux, and where surface temperature is high, which enhances the upward flux of longwave radiation. These conditions are met in desert regions. In the polar regions, cloud cover is also low but since surface temperature is low as well (most of the shortwave radiation is reflected instead of being absorbed), the net longwave loss at the surface is modest. However, the annual average Lw_{net} loss in some parts of the polar regions is sufficiently large to result in a net radiation loss, e. g., over large parts of the interior Greenland and Antarctic Ice Sheets ($R = Shw_{\text{net}} + Lw_{\text{net}} < 0$, Fig. 6.7c). This negative net radiation is remarkable, and greatly influences the near surface climate; see the following sections.

6.5.4 Turbulent Fluxes

In the polar regions the net radiative flux is zero to negative in winter, and over the large ice sheets of Greenland and Antarctica it is zero to negative averaged over the year. Since the heat flux from the snowpack to the surface is on an annual basis small, there must be a quasi-continuous heat source from the atmosphere to the surface to balance the negative net radiative flux. The existence of this heat source is also evident from the fact that in the winter months, in the absence of significant

incoming shortwave radiation, near surface temperature does not show a continuous decrease but rather reaches a quasi-steady state. The heat source resupplying the heat lost through the negative surface radiative balance must be in the form of turbulent transport of sensible and/or latent heat.

Fluid motions are turbulent when they are disordered, and are typically associated with irregular, eddying motion. This is commonly experienced on a windy day, when gusts of wind represent the effects of turbulence. But even on a calm day, the flow is turbulent, when seen on a sufficiently large scale. Turbulence occurs in fluid motions when the Reynolds number (see (1.31)), a dimensionless measure of the velocity, is sufficiently large. In convective motions driven purely by buoyancy (such as commonly observed atmospheric thermals), the convective velocities are controlled by the amount of heating of the ground or ocean surface due to absorption of solar radiation, which causes unstable density differences to occur.

In turbulent flows, the vertical flux of a quantity c is given by the expression $\overline{w'c'}$, where the primes denote the turbulent fluctuations about the mean value, w presents vertical wind velocity, and the overbar denotes the average, for example a local time average.

We are interested in assessing the vertical transport of sensible heat and latent heat. To do this, we first define the potential temperature θ; this is the temperature an air parcel would have when brought adiabatically (i. e., without heat exchange with its environment) from a location with pressure p and temperature T to a reference pressure p_0. Potential temperature is defined as

$$\theta = T \left(\frac{p_0}{p} \right)^{R_d/c_p}, \tag{6.7}$$

where R_d is the gas constant for dry air and c_p the specific heat capacity of air at constant pressure. In an adiabatic atmosphere (which approximately represents the state of the troposphere), the potential temperature is constant; therefore, vertical heat fluxes are associated with fluctuations about this constant adiabatic state.

In a moist atmosphere, the latent heat is proportional to the water vapour content, measured as the specific humidity q, which is the mass fraction of water vapour in the air. Vertical upward fluxes of sensible heat H and latent heat LE at the Earth's surface are thus defined by

$$H = \rho c_p \left(\overline{w'\theta'} \right)_s, \quad LE = \rho L_{v,s} \left(\overline{w'q'} \right)_s, \tag{6.8}$$

where the subscript s on the fluxes refers to the surface, ρ is air density, w', θ' and q' are the turbulent fluctuations of vertical wind, potential temperature and specific humidity, and $L_{v,s}$ is the latent heat of vapourisation (v) or sublimation (s).

The turbulent fluxes can be estimated using so-called first-order closure, which defines turbulent diffusion coefficients (eddy diffusivities) to relate the turbulent fluxes to the local mean gradient of potential temperature and specific moisture. The turbulent fluxes are then written as

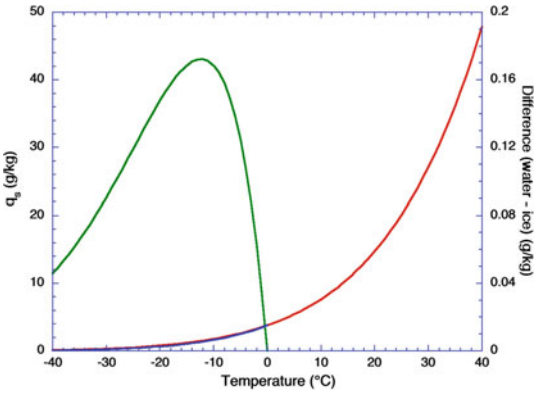

Fig. 6.9 Saturated specific humidity q_s over water (red, left scale), over ice (blue, left scale), and the difference between them (green, right scale) as a function of temperature

$$H \approx -\rho c_p K_h \frac{\partial \theta}{\partial z}, \quad LE \approx -\rho L_{v,s} K_q \frac{\partial q}{\partial z}, \tag{6.9}$$

where $K_{h,q}$ is the turbulent diffusion coefficient for heat (h) or moisture (q). Note that $K_{h,q}$ is not a property of the fluid but of the flow. These equations show that the fluxes can be calculated using the (measured) vertical gradients of temperature and moisture content.

Figure 6.3 shows that, when averaged over the globe and year, both turbulent fluxes provide an energy loss for the surface. In the polar regions the opposite must be true: here, the turbulent heat fluxes must act as a source of energy to balance the surface radiation deficit. According to (6.9), this implies that the near surface potential temperature and specific moisture content must be higher than at the surface. Because of the low temperatures, the specific moisture and hence its gradients are small in the polar regions (Fig. 6.9). As a result, the latent heat flux is on average small. It is mainly the turbulent flux of sensible heat that balances the radiative heat loss (Fig. 6.10). The only way this can be achieved is when the atmosphere is warmer than the surface, i. e., through the existence of a quasi-permanent surface temperature inversion.

6.6 Temperature Inversion and Katabatic Winds

6.6.1 Surface Temperature Inversion and Deficit

A temperature inversion is defined as an increase in temperature with altitude, which constitutes a reversal of the general decrease in temperature with height in the troposphere. The existence of a surface-based temperature inversion over a glacier or ice sheet can be the result of two different processes: (1) a radiation deficit at the surface; (2) warm air overlying a melting snow/ice surface.

As demonstrated in the previous section, the annual average net incoming radiation over polar glaciers and ice sheets is zero or negative. When there is significant wind shear, this heat loss is balanced by the turbulent transport of sensible heat from

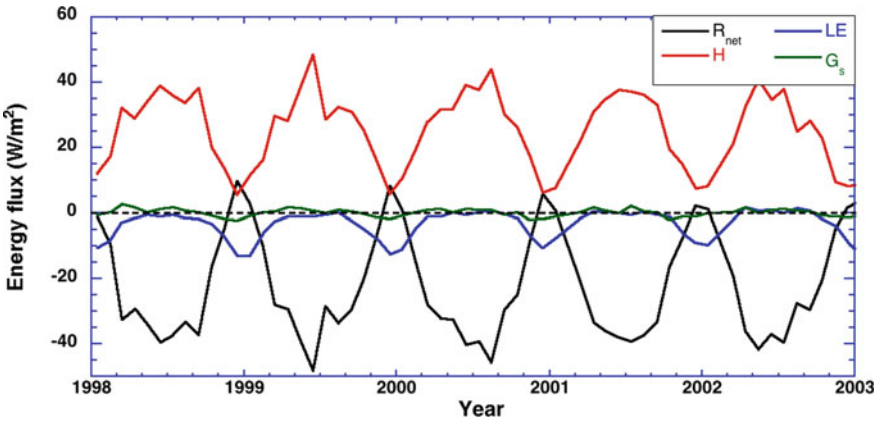

Fig. 6.10 Example of time series of the surface energy balance (based on monthly means) derived from automatic weather station observation at site AWS 6 in Dronning Maud Land, Antarctica [4]. R_{net} is the net (combined short- and long-wave) radiation, H and LE the sensible and latent heat respectively, and G_s the sub-surface heat flux

the air to the surface, which cools the air and heats the surface. In case of low or zero wind speed, the generation of turbulence is suppressed so that (during winter) there are only the subsurface heat flux and incoming longwave radiation from the atmosphere to act as heat sources. Because the surface radiates as a black body, and the (cloudless) sky radiates as a grey body with typical emissivities of 0.6–0.7, the surface temperature must be considerably lower than the near surface air temperature in order to balance the incoming radiation. Note that the temperature inversion forming due to a radiation deficit at the surface is not limited to the polar regions but is also observed during clear nights at lower latitudes. The polar temperature inversion is, however, more persistent and stronger. The persistent temperature inversion will weaken or disappear completely due to heating of the surface by solar radiation. Other processes reducing the inversion strength are mixing through shear turbulence (i. e., increasing wind speed) and cloud formation, which increases the atmospheric emissivity.

The second process resulting in a surface based temperature inversion occurs when warm air (temperature $> 0\,^{\circ}\text{C}$) overlies a melting snow or ice surface of which the surface temperature is restricted to $0\,^{\circ}\text{C}$. This type of temperature inversion persists throughout the day and summer whenever the surface is melting, and can be found over glaciers, the margins of the Greenland Ice Sheet, and in the Antarctic Peninsula.

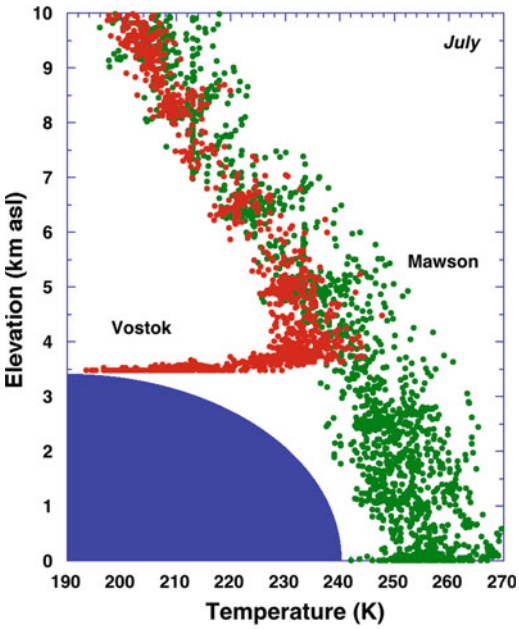

Fig. 6.11 Six years of winter (July) temperature observations at two Antarctic stations, Vostok and Mawson

Figure 6.11 presents an example of observed winter (July) temperature profiles for two stations on the Antarctic Ice Sheet, Vostok and Mawson. Vostok is an inland station on the Antarctic plateau, while Mawson is a coastal station. The figure shows that in the free atmosphere the temperature only slightly decreases from the coast towards the interior of Antarctica. The strong decrease of surface temperature from the coast towards the high plateau is therefore almost entirely determined by the stronger surface temperature inversion. The stronger inversion at Vostok is due to the lower wind speeds and cloud cover at that location. Mawson is located at the foot of the ice sheet and experiences more clouds and strong winds that effectively mix the air near the surface and prohibit the formation of a strong temperature inversion.

A common measure of the strength of the surface based temperature inversion (ΔT_{inv}) is the difference between the (near) surface temperature and the highest temperature observed in the lower atmosphere (Fig. 6.12a). However, high resolution vertical profiles are rare, and atmospheric models usually do not have sufficient vertical resolution for this method. An alternative is to extrapolate the background (potential) temperature profile to the surface and calculate the difference with the actual surface (potential) temperature (Fig. 6.12). The resulting quantity is defined as the surface (potential) temperature deficit ΔT_s ($\Delta \theta_s$), which is strictly seen to be not equal to ΔT_{inv}.

Figure 6.13 illustrates the resulting temperature deficit over the polar regions in winter. Over the north polar basin the wintertime temperature deficit is 15–20 K, over thick sea ice that effectively insulates the atmosphere from the warm ocean.

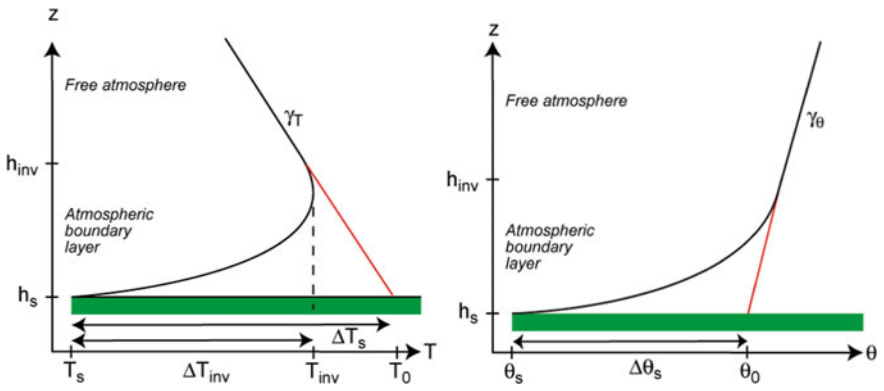

Fig. 6.12 Schematic illustration of the surface temperature inversion ΔT_{inv} and surface (potential) temperature deficit ΔT_s ($\Delta\theta_s$). T_s (θ_s) denotes the surface (potential) temperature, h_s the surface height and h_{inv} the height of the inversion layer. γ_T (γ_θ) denotes the (potential) temperature equilibrium gradient (lapse rate) in the free atmosphere. The (potential) temperature deficit at the surface can be determined by extrapolating the (potential) temperature profile in the free atmosphere to the surface (T_0 and θ_0)

Further to the south, the temperature inversion disappears and the deficit becomes negative in areas where cold continental air is advected over warm ocean water. This mainly occurs east of the continents due to the average westerly circulation. The sea ice marks the edge of the surface inversion, which accounts for a large part of the horizontal temperature gradients.

Over the Antarctic region a significant part of the variation in the temperature at the surface is due to variations in the inversion strength. Strong inversions are found over the large ice shelves and the high plateau. Due to increased wind speeds, the temperature inversion strength is directly related to the surface slope, i. e., the presence of strong katabatic winds. The temperature inversion on the Antarctic plateau is

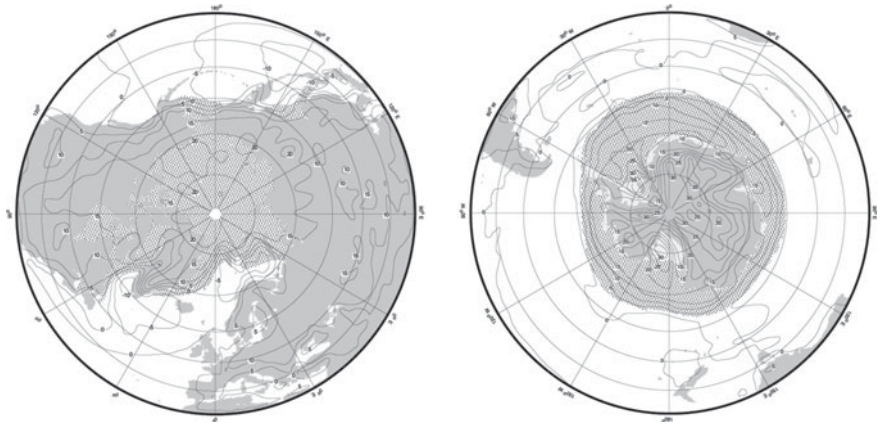

Fig. 6.13 Multi-year average potential temperature deficit at the surface in winter for the north (left) and south (right) polar regions (based on ECHAM4 data)

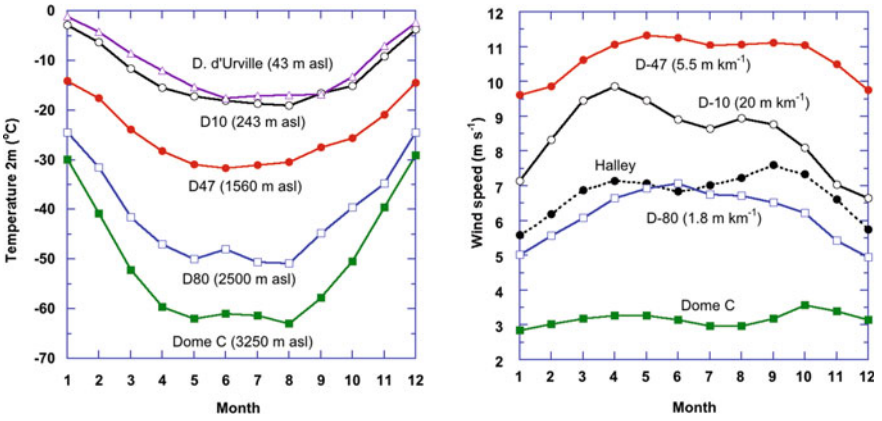

Fig. 6.14 Annual cycle of near-surface temperature (left) and wind speed (right) at a series of weather stations in Adélie Land, Antarctica [6]. Dome C is situated on a dome and Halley on an ice shelf, where there is no or only a very small surface slope

much stronger than over the Greenland Ice Sheet, because the latter experiences regular warm air advection events. In summer, when the radiation deficit becomes small or vanishes, the temperature inversion is (partially) destroyed. The strength of the surface temperature inversion in winter therefore explains (part) of the differences in amplitude of the annual temperature cycle, as seen in Fig. 6.14a.

6.6.2 Katabatic Winds

Katabatic winds are forced by gravity that acts on cold dense air that is formed by the quasi-continuous sensible heat transport to the surface. For this reason, katabatic winds always occur in combination with a surface temperature deficit. Another prerequisite for well developed gravity winds is that the surface has a significant slope. This is the case for valley glaciers and the margins of ice sheets and ice caps. Because the forcing is largest at the surface, where the wind speed is by definition zero, the wind speed attains a maximum at some height above the surface. We distinguish two types of katabatic flows based on the forcing mechanism of the temperature deficit at the surface: (1) forced by a radiation deficit at the surface, and (2) forced when warm air overlies a melting snow/ice surface. The first type requires that the amount of solar insolation must be limited, and is therefore especially well developed during the long polar nights over the large ice sheets. Due to the large time scale involved, the Coriolis force is in this case an important term in the momentum balance, deflecting the wind in the cross slope direction, towards right in the NH, towards left in the SH. The second type requires the presence of air with a temperature $> 0\,°C$ over a melting ice surface. This type therefore persists throughout the day and summer whenever the ice/snow surface is at the melting point. It has a smaller time scale in which to develop, which makes the Coriolis force less important in the momen-

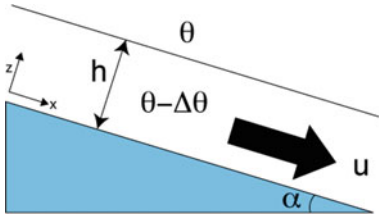

Fig. 6.15 Schematic illustration of the two-layer Ball model

tum balance and the wind direction will be directed more downslope. This type is sometimes referred to as glacier wind.

The general features of katabatic winds can be illustrated with the Ball model [7], in which the strength and the direction of the flow are directly linked to the strength of the surface temperature deficit and the surface slope. The Ball model is a two-layer model (see Fig. 6.15) in which the upper layer represents the free atmosphere with a potential temperature θ and large scale pressure gradient (expressed by geostrophic flow strength, (fu_g, fv_g)). The lower layer is the katabatic layer with a potential temperature $\theta - \Delta\theta$, where $\Delta\theta$ represents the potential temperature deficit of the lower layer. In addition, h is the thickness of the katabatic layer, α is the surface slope, and u is the down-slope and v the cross-slope wind. Due to the choice of the Cartesian coordinate system with the x-axis oriented downslope, a thermodynamic forcing term F is introduced in the downslope component of the momentum equation:

$$F = g\frac{\Delta\theta}{\theta}\sin\alpha; \tag{6.10}$$

this term represents the katabatic forcing. Assuming friction to be proportional to the square of the velocity, stationarity ($\partial u/\partial t = \partial v/\partial t = 0$), negligible large scale forcing ($u_g = v_g = 0$), and homogeneity in the horizontal, the momentum equations reduce to

$$\begin{aligned} 0 &= fv - \frac{k}{h}Vu + g\frac{\Delta\theta}{\theta}\sin\alpha, \\ 0 &= -fu - \frac{k}{h}Vv, \end{aligned} \tag{6.11}$$

where the first terms represent the Coriolis acceleration, and the second terms represent simple friction, where $V = \sqrt{u^2 + v^2}$ is the absolute velocity and k is the drag coefficient. If we assume that u and v can be expressed in terms of the absolute velocity V and the angular deviation from the fall line ϕ, thus $u = V\cos\phi$ and $v = V\sin\phi$, we can solve this set of equations:

$$\begin{aligned} V^2 &= \frac{\left[F^4 + 4k'^2F^2\right]^{1/2} - f^2}{2k'^2}, \\ \cos\phi &= \frac{k'V}{\left[f^2 + k'^2V^2\right]^{1/2}}. \end{aligned} \tag{6.12}$$

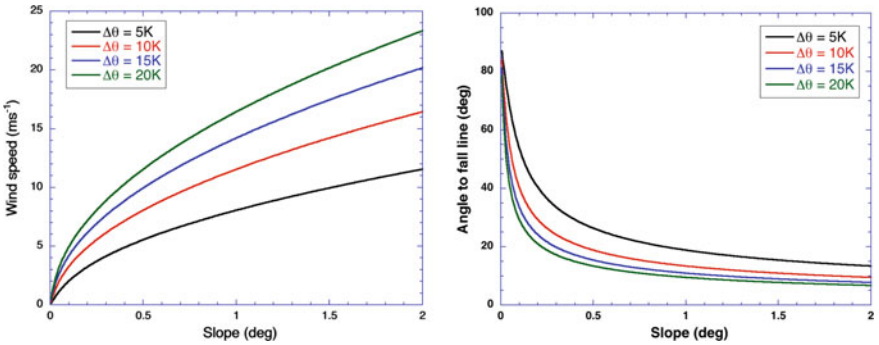

Fig. 6.16 Results of the Ball model as a function of slope angle and strength of the deficit, with $u_g = v_g = 0$, $\theta = 255$ K, $k = 0.005$, $h = 100$ m

Here, $k' = k/h$ and $F = g(\Delta\theta/\theta)\sin\alpha$.

Figure 6.16 presents this solution for different values of $\Delta\theta$. The figure shows that wind speed increases with increasing slope and strength of the deficit. When wind speed increases, the effect of friction increases as does the effect of the Coriolis turning. The latter deflects the wind from the fall line while friction turns it towards the fall line. Since friction dominates the Coriolis effect, the deviation from the fall line decreases with increasing wind speed. When applying this model on the Antarctic Ice Sheet with a prescribed $\Delta\theta$, the resulting flow lines correspond reasonably well with the observed flow patterns.

A useful tool to detect persistent katabatic winds is the directional constancy (dc), which is defined as the ratio of vector mean wind speed over the mean absolute wind speed:

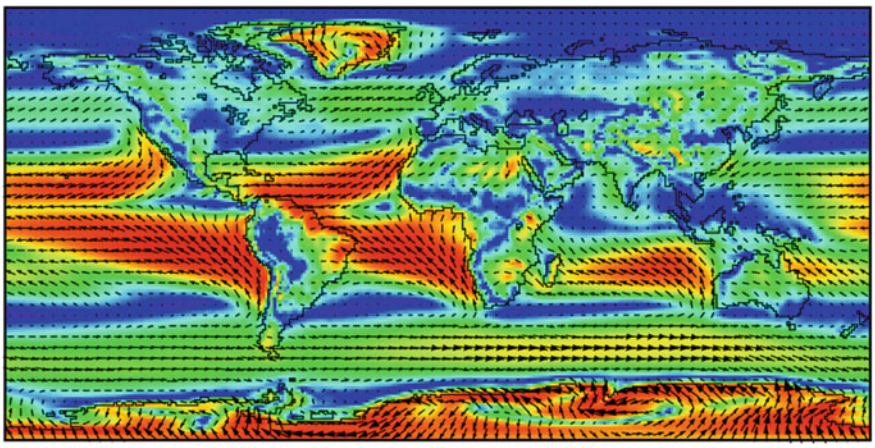

Fig. 6.17 Directional constancy ranging from 0.35 (blue) to 0.99 (red), and 10 m wind vectors, where the longest vectors represent 15 m s^{-1} wind speed (based on ECHAM4 data)

$$dc = \frac{(\overline{u}^2 + \overline{v}^2)^{1/2}}{\overline{(u^2 + v^2)^{1/2}}}, \tag{6.13}$$

where u and v are the zonal and meridional wind components, respectively. Note that dc varies between 0 and 1, where a value of 1 denotes wind from a single well-defined direction. High values of dc often express the dominance of one forcing mechanism over other mechanisms. Figure 6.17 shows the global distribution of the mean wind vector and magnitude of dc. The important wind systems are clearly visible, i. e., the trade winds on either side of the equator, the westerlies in the mid-latitudes and the well developed katabatic winds over the Greenland and Antarctic Ice Sheets, with its clear anti-cyclonic rotation due to the Coriolis deflection.

Katabatic winds exhibit temporal variations related to variations in the surface temperature deficit, as illustrated with the Ball model. Over the large ice sheets the temperature inversion has a strong annual cycle and nearly disappears in summer. Figure 6.14b shows for Antarctica that this is indeed the case, although the figure also shows that other processes are active. At the inland site Dome C, the surface is approximately flat and no katabatic forcing is present: the winds are forced by the large scale pressure gradient. Because the large scale pressure gradients are weak over the continent (see Fig. 6.5), the winds are also weak near the surface. At Halley, the other station without surface slope and thus katabatic forcing, the wind speed is determined by the coastal large scale pressure gradient, forcing easterly winds. On the slopes of the ice cap (sites D-10, D-47 and D-80), katabatic forcing dominates the wind, although large scale forcing is approximately equally important in summer when the surface temperature inversion becomes weak. Note that the wind speed does not increase indefinitely when slope increases: at D-10 the slope is the largest but wind speed has decreased compared to D-47. This is due to the significant thickening of the boundary layer towards the coast where the shallow katabatic layer must merge with the marine boundary layer over the ocean.

An interesting feature is observed in the ablation zone of the Greenland Ice Sheet, where both katabatic and glacier winds occur. In winter the situation is comparable to Antarctica and strong katabatic winds are forced through a radiation deficit at the surface. In summer, when the surface melts and cannot raise its temperature, persistent glacier winds are forced. As a result the wind speed and directional constancy peak twice each year.

6.7 Precipitation

The surface mass balance (SMB) of a glacier is defined as the sum of all processes adding mass to the surface (accumulation) minus all processes removing mass (ablation):

$$\mathrm{SMB} = \int_{1\ \mathrm{yr}} (\mathrm{SN} + \mathrm{RF} - \mathrm{SU_s} - \mathrm{SU_{ds}} - \mathrm{ER_{ds}} - \mathrm{RU})\ dt. \tag{6.14}$$

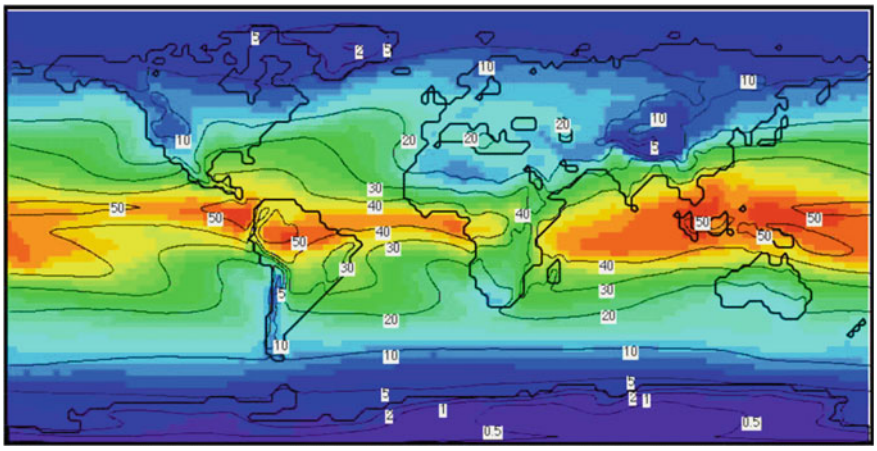

Fig. 6.18 Annual mean precipitable water vapour (PW) [(mm, see (6.15)] (based on ECHAM4 data)

Accumulation is often defined as snowfall (SN) minus sublimation (SU). Removal of mass occurs by means of surface sublimation (SU_s), sublimation of drifting snow (SU_{ds}), erosion by drifting snow (ER_{ds}), and melt and subsequent runoff (RU). RF represents refreezing of rainfall. The surface mass balance is usually expressed in metres water equivalent per year (m w.e. y^{-1}). The SMB is discussed in Chap. 7; here we will focus on precipitation, the most important positive component of the SMB.

Snowfall constitutes the largest contribution to the accumulation over a glacier and ice sheet. Other precipitation components that contribute positively to the surface mass balance are hail and undercooled water droplets that freeze upon impact with the surface. The maximum possible amount of precipitation depends on the total amount of moisture in the atmosphere, which strongly depends on temperature as shown in Fig. 6.9. As a result nearly all water vapour is concentrated in the lowest kilometres of the atmosphere. Furthermore, due to the low temperatures in the polar regions the moisture content there is extremely low.

The lack of moisture in the atmosphere over the large ice sheets becomes evident when looking at the annual mean of the total precipitable water PW, i. e., the column abundance of moisture (both liquid and vapour):

$$\mathrm{PW} = \int_0^\infty \rho_v \, dz = \int_0^\infty \rho q \, dz \approx \frac{1}{g} \int_0^{p_s} q \, dp, \tag{6.15}$$

where ρ_v is water vapour density (in kg m^{-3}), $q = \rho_v/\rho$ is the specific humidity, g is gravity, and PW is in units of mm or kg m^{-2}. Note that for PW to actually rain out, lifting of the air parcels is necessary. This either occurs by spontaneous convection or by frontal convection.

It is clear from Fig. 6.18 that the tropics are moisture production regions. The air at higher latitudes has cooled so much that its moisture content is low: most of the water

vapour produced by evaporation at the surface in the tropical regions has condensed and rained out at lower latitudes, for instance via the mid-latitude storm tracks. In the polar regions the surface air layer just above the sea or snow or ice surface is always saturated. However, this does not lead to strong sublimation because the amount of available energy to heat the surface is limited (large incidence angle of the solar radiation and high surface albedo). Furthermore, the presence of the persistent surface based temperature inversion suppresses sublimation/evaporation. In case of a melting surface, the moisture gradient may reverse and evaporation is suppressed as well. As a result, the vertical transport of moisture from the surface to the atmosphere is small in the polar regions. The lower values of PW over the Antarctic plateau compared to the Greenland Ice Sheet are due to the higher elevation and lower temperatures over Antarctica. Due to the lack of energy to heat the surface, spontaneous convection is weak and infrequent poleward of 75° N and 60° S, apart from at the sea ice edge and continental margins, for example. Precipitation is therefore mostly the result of forced convection, i. e., frontal activity, and large scale circulation in combination with (ice sheet) topography.

The spatial distribution of precipitation in the Arctic region is determined by the average flow direction and orography. We find precipitation maxima in areas where humid air transported by the flow encounters topographical barriers, such as at the west coast of the U. S. A., the west coast of Norway, and the south coast of Iceland, all major glacierised regions of the Northern Hemisphere. For all these locations a significant part of the precipitation falls as rain; only over the interior of the Greenland Ice Sheet does almost all precipitation fall as snow. The north polar basin is fairly dry (< 250 mm w.e.) and here also a significant amount of that precipitation falls as rain (10–40%).

In the Antarctic region the mean flow is more zonally oriented and so is the precipitation distribution. Significant topographical barriers in the westerly flow are the Chilean Andes, New Zealand Alps and the Antarctic Peninsula. Due to its high elevation, the Antarctic continent also acts as a barrier for further southward transport of moisture. As a result, the interior Antarctic Ice Sheet is very dry and is often referred to as a polar desert. Over the Antarctic continent and its immediate surroundings essentially all precipitation falls as snow. The variability in the precipitation can be explained to a large extent by the circulation patterns induced by the circumpolar pressure trough. Most precipitation falls in the coastal areas and on the leeward side of the climatological low pressure areas.

Note that these maps are based on averages over many years. Precipitation events are in general very irregular in space and time. On Antarctica, the total amount of annual snowfall might fall in a few major events. As a result, individual annual layers within ice cores do not necessarily represent climatic information for a whole year.

6.8 Notes and References

Table 6.2 gives values of the constants used in this chapter.

Table 6.2 List of constants and their values as used in this chapter

Name	Symbol	Value
Speed of light	c	2.998×10^{8} m s^{-1}
Planck constant	h	6.63×10^{-34} J s
Boltzmann constant	k	1.38×10^{-23} J K^{-1}
Latent heat of melt (ice $\leftrightarrow$ water)	L_m	3.34×10^{5} J kg^{-1}
Latent heat of sublimation (ice $\leftrightarrow$ vapour)	L_s	2.84×10^{6} J kg^{-1}
Latent heat of evaporation (water $\leftrightarrow$ vapour)	L_v	2.51×10^{6} J kg^{-1}
Solar constant	S_0	1366 W m^{-2}
Specific gas constant, dry air	R_d	287.05 J kg^{-1} K^{-1}
Specific gas constant, moist air	R_v	462 J kg^{-1} K^{-1}
Specific heat of air at constant pressure	c_p	1004 J kg^{-1} K^{-1}
Stefan Boltzmann constant	σ	5.67×10^{-8} W m^{-2} K^{-4}

The values of L_m and R_v are for note, as they are not referred to in the text

There are several source texts which cover most of the material in this chapter. Wallace and Hobbs [8] give a complete review of the principles of meteorology, including chapters on atmospheric dynamics, weather systems, the planetary boundary layer (the lowest kilometre where the effects of friction are important), and climate dynamics. One of the sections in the last chapter carries the provocative but faux-naïf title, 'Is human-induced greenhouse warming already evident?' The earlier part of the book covers the carbon cycle and the hydrologic cycle, principles of radiative transfer, atmospheric thermodynamics, and cloud physics.

A more comprehensive treatment of radiative transfer theory is given in the book by Liou [9]. This book takes the reader through the basic physical processes of absorption, emission and scattering, and gives an overview of atmospheric processes of gaseous absorption and particulate scattering. The last part of the book focuses on practical applications of radiative transfer theory to remote sensing, and the inclusion of radiative processes in climate models.

The book by King and Turner [10] gives a comprehensive survey of the meteorology in Antarctica, including extensive discussion of observational processes, physical climatology, and the general circulation and synoptic meteorology. There is also a thorough discussion of mesoscale processes, including in particular katabatic winds.

Exercises

6.1 *The Planck radiation curve (this is really five separate questions)*

(a) The Planck radiation curve is given by the formula in (6.1):

$$F_\lambda(T) = \frac{2\pi hc^2}{\lambda^5\left(e^{hc/k\lambda T} - 1\right)},$$

and its integral with respect to wavelength λ gives the emitted radiation as in (6.2):

$$F(T) = \int_0^\infty F_\lambda(T)\, d\lambda = \int_0^\infty \left[\frac{2\pi hc^2}{\lambda^5\left(e^{hc/k\lambda T} - 1\right)}\right] d\lambda.$$

By choosing a suitable substitution of the integration variable, show that

$$F(T) = \sigma T^4, \quad \sigma = \frac{2\pi k^4 I}{h^3 c^2}, \quad I = \int_0^\infty \frac{\theta^3\, d\theta}{e^\theta - 1}.$$

(b) To evaluate the integral, show that

$$\frac{1}{e^\theta - 1} = e^{-\theta}(1 - e^{-\theta})^{-1},$$

expand the second term as a geometric series (note that $e^{-\theta} < 1$ if $\theta > 0$), and hence show that

$$I = \sum_1^\infty \int_0^\infty \theta^3 e^{-n\theta}\, d\theta.$$

By a suitable rescaling of θ, deduce that

$$I = \Gamma(4)\sum_1^\infty \frac{1}{n^4}, \quad \Gamma(z) = \int_0^\infty t^{z-1}e^{-t}\, dt$$

(this is the *gamma function*). Show that $\Gamma(1) = 1$. By using integration by parts, show that for $z > 0$ (or more generally $\mathrm{Re}\, z > 0$) $\Gamma(z+1) = z\Gamma(z)$, and deduce that for integer values of n, $\Gamma(n+1) = n!$. Hence find the value of $\Gamma(4)$.

(c) Next, let us recall the Fourier series of a function $f(x)$ defined on $(-\pi, \pi)$, and which is 2π–periodic:

$$f(x) = \sum_{-\infty}^\infty a_n e^{inx}.$$

Noting that $\int_{-\pi}^{\pi} e^{imx}\,dx = 0$ for integers $m \neq 0$, but $= 2\pi$ if $m = 0$, show that

$$a_n = \frac{1}{2\pi}\int_{-\pi}^{\pi} f(x)e^{-inx}\,dx.$$

Deduce *Parseval's formula*:

$$\frac{1}{2\pi}\int_{-\pi}^{\pi} |f(x)|^2\,dx = \sum_{-\infty}^{\infty} |a_n|^2.$$

(d) Show that $\sinh i\xi = i\sin\xi$, $\cosh i\xi = \cos\xi$. Deduce that for integer values of n, $\sinh(-in\pi) = 0$, $\cosh(-in\pi) = (-1)^n$.
Show that $\int_{-\pi}^{\pi} e^{zx}\,dx = \frac{2}{z}\sinh\pi z$.
By differentiating twice, show that

$$\int_{-\pi}^{\pi} x^2 e^{zx}\,dx = \frac{2\pi^2}{z}\sinh\pi z - \frac{4\pi}{z^2}\cosh\pi z + \frac{4}{z^3}\sinh\pi z.$$

Hence show that

$$\int_{-\pi}^{\pi} x^2 e^{-inx}\,dx = \frac{4\pi(-1)^n}{n^2},\ n \neq 0, \quad = \frac{2\pi^3}{3},\ n = 0.$$

Derive the Fourier coefficients for $f(x) = x^2$, and by using Parseval's formula, show that

$$\sum_{1}^{\infty} \frac{1}{n^4} = \frac{\pi^4}{90}.$$

(e) Use the values $c = 2.998 \times 10^8$ m s^{-1}, $k = 1.381 \times 10^{-23}$ J K^{-1}, $h = 6.626 \times 10^{-34}$ J s to evaluate the Stefan–Boltzmann constant σ, giving also its units.

6.2 In Fig. 6.2, the caption refers to the fact that the total received solar radiation at ToA is 1366 W m^{-2}. However, the area under the solar Planck curve in the figure is approximately 593 W m^{-2}. To explain this, follow the steps below.

(a) Use the units of h, c given in Exercise 6.1 to show that F_λ in equation (6.1) has units W m^{-3}, and deduce that λF_λ has units of W m^{-2}, as does $F(T)$ given in equation (6.2).
Show that $\log_{10}\lambda = \frac{\ln\lambda}{\ln 10} \approx 0.43\ln\lambda$.
Hence show that

$$\int_0^{\infty} F_\lambda\,d\lambda = \int_0^{\infty} \frac{\lambda F_\lambda\,d\lambda}{\lambda} = \int_{-\infty}^{\infty} \lambda F_\lambda\,d\ln\lambda = \ln 10\int_{-\infty}^{\infty} \lambda F_\lambda\,d\log_{10}\lambda.$$

Deduce that the area under the curve shown in Fig. 6.2 is

$$\int_{-\infty}^{\infty} \lambda F_\lambda \, d\log_{10}\lambda = 0.43F(T),$$

and deduce its value if $F(T) = 1366$ W m^{-2}.
To verify this value, compute the area of the approximating triangle in Fig. 6.2 whose maximum is at $\lambda F_\lambda = 1000$ W m^{-2} and whose other two vertices are on the $\log_{10}\lambda$ axis at $\lambda = 0.2$ μm and $\lambda = 3$ μm (thus the (dimensionless) length of the base is $\log_{10} 15$), and compare the result with the actual value of 593 W m^{-2}.

(b) Now consider the Earth radiation curve.
First, show that the Planck function can be written in the form

$$\lambda F_\lambda = \frac{F(T)}{I} \frac{\theta^4}{(e^\theta - 1)}, \quad \theta = \frac{hc}{kT\lambda},$$

where I is defined in Exercise 6.1. Using the definitions of the constants there, show that θ is dimensionless, and show also that $d\log_{10}\lambda = -d\log_{10}\theta$.
Show that λF_λ has a maximum where $\theta = 4(1 - e^{-\theta})$, show graphically that the maximum is unique, and show that $\theta \approx 4$. Compute a better approximation by iterating the map $\theta_{n+1} = 4(1 - e^{-\theta_n})$; why does this work?
Deduce that if the ratio of the Earth radiation $F^E(T)$ to the ToA sun radiation $F^S(T)$ is $\frac{1}{4}(1 - \alpha) \approx 0.17$, then the ratio of the maxima of λF_λ^E and λF_λ^S is the same, as is the ratio of the areas under the curves. Using an approximating triangle to the Earth curve in Fig. 6.2 with maximum at 170 W m^{-2} and vertices on the $\log_{10}\lambda$ axis at $\lambda = 5$ μm and $\lambda = 75$ μm (so the dimensionless length of the base is $\log_{10} 15$), show that the ratio of this estimate to your estimate for the area under the sun radiation curve is also 0.17.

6.3 *The total cloud effect and the radiation paradox*
We look at the influence of clouds on the surface radiation budget. In this exercise we do this by comparing the net surface radiation (R_{net}) during clear sky conditions with the average situation (with clouds); the difference is called the 'total cloud effect'. Figure 6.19 shows the total cloud effect averaged over the year.

(a) What are the components of the total cloud effect, and what meteorological variables influence these components at first order? Which component would you expect to dominate over dark surfaces? Is this confirmed in the figure? In that case, how is the total cloud effect related to surface temperature?

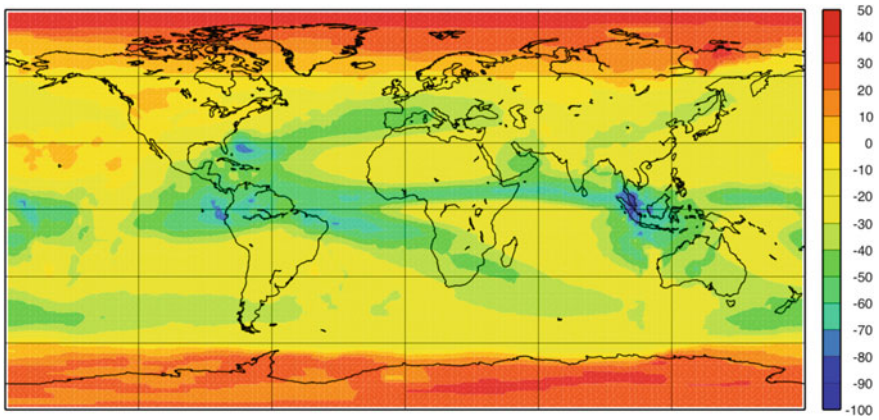

Fig. 6.19 Total cloud effect (i. e., $R_{\text{net}}^{\text{cloudy}} - R_{\text{net}}^{\text{clear sky}}$, W m^{-2}) [3]

(b) Explain the patterns in the polar regions depicted in the figure. The increase of net surface radiation as an effect of clouds is sometimes called the radiation paradox. Do you think this is a good name?
Use Fig. 6.20 to answer the following questions. Observations at the Antarctic research station Neumayer (70° S) suggest that

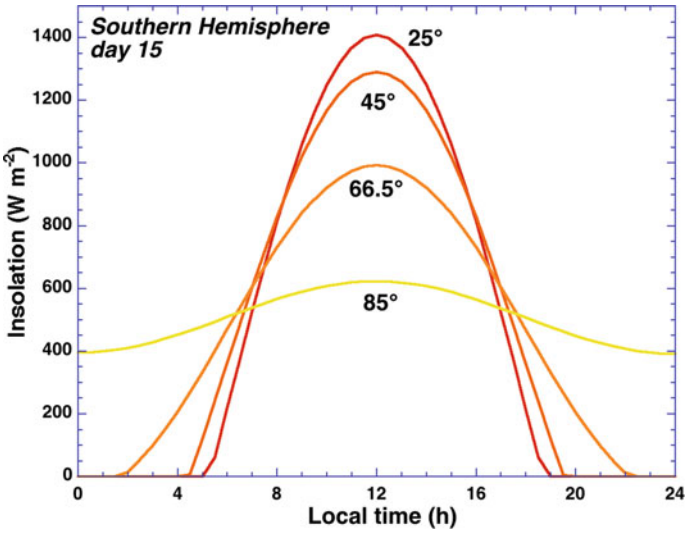

Fig. 6.20 Daily cycle of incoming Shw at ToA, for four SH latitudes on 15 January

$$LW_{\text{in}}(z=0) = \varepsilon_a \sigma T_a^4 \approx (0.765 + 0.22N^3)\sigma T_a^4,$$

where ε_a is the effective atmospheric emissivity, T_a is air temperature at 2 m and N is cloud cover (a number between 0 and 1). Noon of 15 January 2000 is windless and sunny at Neumayer. The atmospheric transmissivity for shortwave radiation $\tau_{SW} = 0.8$, and the temperature near the snow surface, which has an albedo of 0.85, has risen to as high as $-3\,^\circ$C. Lying on his therm-a-rest, glaciologist Gerd Gernknödel is taking a sunbath in his bare chest! Suddenly a cloud moves in front of the sun, and τ_{SW} drops to 0.5.

(c) What will happen to the snow surface temperature?
Hint: neglect the temperature difference between 2 m and the surface and assume surface emissivity $\varepsilon_a = 1$. *Further assume that, apart from the radiation balance, no other terms in the surface energy balance play a rôle.*

(d) Does Gerd need a jacket?
Hint: calculate the radiation balance of Gerd's skin, assuming radiative equilibrium at skin temperature when he feels comfortable and take $\varepsilon_{Gerd} = 1$. *Take a value of* $32\,^\circ$C *as Gerd's skin temperature.*

References

1. Fowler A (2011) Mathematical geoscience. Springer, London
2. Trenberth K, Fasullo J, Kiehl J (2009) Earth's global energy budget. Bull Amer Met Soc 90(3):311–323
3. Hatzianastassiou N, Matsoukas C, Hatzidimitriou D, Pavlakis C, Drakakis M, Vardavas I (2004) Ten year radiation budget of the Earth: 1984–93. Int J Climatol 24:1785-1802
4. van den Broeke MR, Reijmer CH, van As D, van de Wal RSW, Oerlemans J (2005) Seasonal cycles of Antarctic surface energy balance from automatic weather stations. Ann Glaciol 41:131–139
5. van den Broeke MR, Smeets CJPP, van de Wal RSW (2011) The seasonal cycle and interannual variability of surface energy balance and melt in the ablation zone of the west Greenland ice sheet. The Cryosphere 5:377–390
6. Turner J, Colwell SR, Marshall GJ, Lachlan-Cope IA, Carleton AM, Jones PD, Lagun JV, Reid PA, Iagovkina S (2004) The SCAR READER project: toward a high-quality database of mean Antarctic meteorological observations. J Clim 17:2890–2898
7. Ball FK (1960) Winds on the ice slopes of Antarctica. In: Antarctic meteorology, proceedings of the symposium held in Melbourne, February 1959. Pergamon Press, Oxford, pp 9–16
8. Wallace JM, Hobbs PV (2006) Atmospheric science: an introductory survey, 2nd edn. Academic Press, Burlington, MA
9. Liou KN (2002) An introduction to atmospheric radiation, 2nd edn. Academic Press, New York
10. King J, Turner J (1997) Antarctic meteorology and climatology. CUP, Cambridge